Multidisciplinary | Rapid Review | Open Access Journal

Date of publication xxxx 00, 0000, date of current version xxxx 00, 0000.

Digital Object Identifier 10.1109/ACCESS.2017.Doi Number

A Hybrid Active Contour Segmentation Method for Myocardial D-SPECT Images

CHENXI HUANG[1], XIAOYING SHAN[2], YISHA LAN[1], LU LIU[3], HAIDONG CAI[4], WENLIANG CHE[3], YONGTAO HAO[1], YONGQIANG CHENG[4], YONGHONG PENG[5](MEMBER, IEEE)

[1]Department of Computer Science and Technology, Tongji University, Shanghai 201804, P. R. China
[2]Normal College, Jiaxing University, Jiaxing, Zhejiang 314001, P. R. China
[3]Department of Cardiology, Shanghai Tenth People's Hospital, Tongji University School of Medicine, Shanghai, 200072, P. R. China
[4]Department of Nuclear Medicine, Shanghai Tenth People's Hospital, Tongji University School of Medicine, Shanghai, 200072, P. R. China
[5]School of Engineering and Computer Science, University of Hull, Hull HU6 7RX, United Kingdom.
[6]Faculty of Computer Science, University of Sunderland, St Peter Campus, SR6 0DD, United Kingdom

Corresponding author: Wenliang Che(chewenliang@tongji.edu.cn), Yongtao Hao (e-mail: hao0yt@163.com) and Yonghong Peng (e-mail:Yonghong.Peng@Sunderland.ac.uk).

The research work presented in this paper was supported by National Science and Technology Support Program (2015BAF10B01); The Natural Science Foundation of China (81670403; 81500381; 81201069).

ABSTRACT Ischaemic heart disease has become one of the leading causes of mortality worldwide. Dynamic single-photon emission computed tomography (D-SPECT) is an advanced routine diagnostic tool commonly used to validate myocardial function in patients suffering from various heart diseases. Accurate automatic localization and segmentation of myocardial regions is helpful in creating a three-dimensional myocardial model and assisting clinicians to perform assessments of myocardial function. Thus, image segmentation is a key technology in preclinical cardiac studies. Intensity inhomogeneity is one of the common challenges in image segmentation and is caused by image artefacts and instrument inaccuracy. In this paper, a novel region-based active contour model that can segment the myocardial D-SPECT image accurately is presented. First, a local region-based fitting image is defined based on information related to the intensity. Second, a likelihood fitting image energy function is built in a local region around each point in a given vector-valued image. Next, the level set method is used to present a global energy function with respect to the neighbourhood centre. The proposed approach guarantees precision and computational efficiency by combining the region-scalable fitting energy (RSF) model and local image fitting energy (LIF) model, and it can solve the issue of high sensitivity to initialization for myocardial D-SPECT segmentation.

INDEX TERMS Myocardium D-SPECT, Image segmentation, Active contour, Level set

I. INTRODUCTION

According to [1], ischaemic heart disease is one of the leading causes of death in the world. Coronary macrovessel stenosis has long been considered the main cause of ischaemic heart disease. Additionally, coronary microvascular dysfunction (CMD) has been demonstrated to play an important role in the occurrence of myocardial ischaemia, resulting in major cardiovascular events or death. Early diagnosis and surgery are measures that can be used to address the health concerns mentioned above. Modern functional medical imaging techniques can contribute significantly to the diagnosis and, in particular, to the quantitative assessment of these diseases [2-3]. At present, various modalities are used in common preclinical cardiac diagnosis, such as single-photon emission computed tomography (SPECT) scans, positron emission tomography (PET) scans, magnetic resonance imaging (MRI), and X-ray computed tomography (CT) [4-7]. Dynamic single-photon emission computed tomography (D-SPECT), which has the capability of estimating extra kinetic information of tissue motion and deformation, is a popular routine diagnostic tool used to evaluate bodily functions affected by various diseases such as pulmonary embolism, pneumonia, heart failure, and tumours.

D-SPECT, shown in Fig. 1, is a special myocardial perfusion imaging device using radionuclide as an imaging diagnostic method. By injecting radionuclide into the blood

This article has been accepted for publication in a future issue of this journal, but has not been fully edited. Content may change prior to final publication. Citation information: DOI 10.1109/ACCESS.2018.2855060, IEEE Access

stream, the blood perfusion and the functional state of heart can be observed via radionuclide myocardial perfusion imaging. Although myocardial perfusion imaging is not a novel technique for the diagnosis of myocardial ischaemia, it is the most reliable and non-invasive method for detecting coronary heart disease by imaging the ischaemia in the myocardium directly. Figure 2 shows examples of cardiac D-SPECT images, including a long-axis and short-axis image. D-SPECT has made considerable progress in imaging devices. Compared with the traditional SPECT of sodium iodide (NaI) crystal, the most advanced, fully digital zinc telluride (CZT) solid-state detector is used in D-SPECT. In D-SPECT, the coronary flow reserve (CFR) is measured by the special treatment software for the heart. CFR can integrate the haemodynamic effects of the epicardial artery, the anterior arteriole, and the arteriole. Furthermore, a comprehensive assessment of the coronary and myocardium can be made, and a reliable basis for the preoperative evaluation and the evaluation of the postoperative curative effect can be provided. The fractional flow reserve (FFR) reflects the influence of the stenosis in an epicardial coronary on the haemodynamics, which has a guiding significance for the clinical profile. Moreover, the coronary flow reserve can provide the comprehensive information of both FFR and microangiopathy (IMR). In future, this detection method is likely to be used more often owing to its safe and reliable non-invasive examination capabilities, as well as high accuracy and sensitivity. In addition, D-SPECT can reduce unnecessary traumatic examination and the corresponding medical expenses for many patients.

FIGURE 1. Images of D-SPECT.

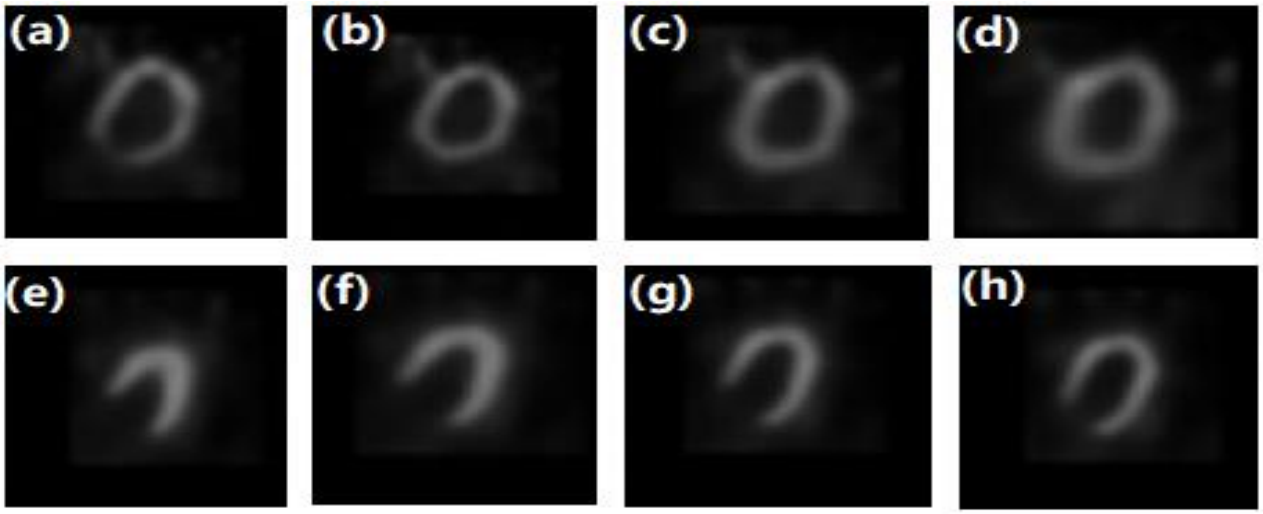

FIGURE 2. Cardiac D-SPECT images. (a) to (d) are short-axis images, and (e) to (h) are long-axis images.

The myocardium is a three-dimensional structure, which cannot be directly visualized using two-dimensional images. With the improvement of temporal and spatial resolution of medical images, D-SPECT images contain substantial information, which makes image processing time-consuming and labourious. Accurate automatic localization and segmentation of myocardial regions is helpful in establishing a three-dimensional myocardial model and assisting clinicians to perform an assessment of myocardial function. However, intensity inhomogeneity, which is caused by image artefacts and instrument inaccuracy, is one of the common issues in image segmentation. Since the introduction by Kass et al. [8], active contour models have become increasingly popular in the field of image segmentation in the past years and can yield closed and smooth contours of the desired objects with promising accuracy [9]. At present, a variety of active contour models have been proposed, such as the Chan-Vese (C-V) model, the geodesic active contour (GAC) model, the active contour model based on cross entropy (CEACM), the local

This article has been accepted for publication in a future issue of this journal, but has not been fully edited. Content may change prior to final publication. Citation information: DOI 10.1109/ACCESS.2018.2855060, IEEE Access

binary fitting (LBF) model, the region-scalable fitting energy (RSF) model, the local image fitting energy (LIF), and the hybrid model with global and local intensity fitting energy (LGIF) model [10-14]. In the C-V model, the global information related to the image, comprising the variances of the pixel greyscale values inside the object region and the background region, is used to guide the curve evolution [15]. However, the interference regions are not separated, which leads to unsatisfactory segmentation results. The global information gained by an edge detector function to drive the evolution of the curve is used in the GAC model. However, the complexity of edge information results in the non-convergence of the GAC model [16]. Compared with the C-V model, the CEACM model replaces the variances with the cross entropies of pixel greyscale values inside the object region and the background region to guide the curve evolution. This model can accurately segment images that are relatively homogeneous, although over-segmentation will occur if the images are less homogeneous. The LBF model, which utilizes the local image information as constraints, can segment objects with intensity inhomogeneities accurately [17-20]. The RSF model, a typical local model, chooses the Gaussian function as the kernel function to calculate the local intensity information. Nevertheless, the convolution is performed in each iteration during the curve evolution, causing massive computational cost. Unlike the RSF model, the convolution is performed before the iteration; thus, the segmentation results of the LIF model are relatively better. The LGIF model is a combination of the C-V model and RSF model, and a series of relatively good segmentation results can be obtained by the LGIF model. However, the computational complexity of hybrid models such as the LGIF model is fairly high. In addition, a heuristic process occurs because several parameters of the hybrid models must be set manually, which leads to increased work [21-23].

In this study, we propose a new model combining the RSF model and LIF model. First, two local intensity fitting functions are defined through the intensity information and local regional differences, which can locally approximate the image intensities on the two sides of the contour in the neighbourhood of every pixel. Next, a likelihood fitting image energy functional is built in a local region around each point. Finally, the level set method is used to present a global energy functional with respect to the neighbourhood centre. The segmentation results are demonstrated by a series of contrasting experiments and a set of metrics, which are used to measure the accuracy of the novel model.

The rest of the paper is organized as follows: Related work is introduced in Section Ⅱ. Our proposed method is described in Section Ⅲ. The experimental results and discussions are given in Section Ⅳ. Finally, we conclude this paper and discuss future work in Section Ⅴ.

II. RELATED WORKS

A. THE RSF MODEL

Consider a vector valued image mapping $\Omega \to \Re^d$, where $\Omega \subset \Re^n$ is the image domain, and $d \geq 1$ is the dimension of a vector $I(x)$. In particular, $d=1$ indicates grey level images, while $d=3$ defines colour images. C is defined as a contour in the image domain Ω [24]. In the RSF model, the local intensity fitting energy for a given point is defined by

$$E_x = \lambda_1 \int_{in(C)} K_\sigma(x-y)\left|I(y)-f_1(x)\right|^2 dy + \lambda_2 \int_{out(C)} K_\sigma(x-y)\left|I(y)-f_2(x)\right|^2 dy \quad (1)$$

where $f_1(x)$ and $f_2(x)$ are two fitting functions that locally approximate the intensity inside and outside the contour C, respectively. λ_1 and λ_2 are two positive constants, and $K(v)$ is a Gaussian kernel function. The total energy function is described as

$$\begin{aligned} E^{RSF}(\phi, f_1(x), f_2(x)) &= \lambda_1 \int \left[\int K_\sigma(x-y)\left|I(y)-f_1(x)\right|^2 H(\phi(y))dy \right] dx \\ &+ \lambda_2 \int \left[\int K_\sigma(x-y)\left|I(y)-f_2(x)\right|^2 H(\phi(y))dy \right] dx \\ &+ \nu \int \left|\nabla H(\phi(x))\right| dx + \gamma \int_\Omega \frac{1}{2}\left(\left|\nabla \phi(x)\right|-1\right)^2 dx \end{aligned} \quad (2)$$

where ϕ is a level set, $H(x)$ is the Heaviside function, and ν and γ are non-negative constants.

The Heaviside function $H(x)$ can be approximated by a smooth function $H_\varepsilon(x)$. It is defined by

$$H_\varepsilon(x) = \frac{1}{2}\left[1+\frac{2}{\pi}\arctan\left(\frac{x}{\varepsilon}\right)\right] \quad (3)$$

and the derivative of H_ε is defined as

$$\delta_\varepsilon(x) = H_\varepsilon'(x) = \frac{\varepsilon}{\pi\left(\varepsilon^2+x^2\right)} \quad (4)$$

For a fixed level set ϕ, we minimize the energy functional in (2) with respect to $f_1(x)$ and $f_2(x)$, and easily obtain

$$f_1(x) = \frac{K_\sigma(x) * \left[H_\varepsilon(\phi(x))I(x)\right]}{K_\sigma(x) * H_\varepsilon(\phi(x))} \quad (5)$$

$$f_2(x) = \frac{K_\sigma(x) * \left[(1-H_\varepsilon(\phi(x)))I(x)\right]}{K_\sigma(x) * \left[1-H_\varepsilon(\phi(x))\right]} \quad (6)$$

Keeping $f_1(x)$ and $f_2(x)$ fixed and using the standard gradient descent method to minimize the energy function with respect to ϕ, the gradient flow function can be obtained as shown below.

This article has been accepted for publication in a future issue of this journal, but has not been fully edited. Content may change prior to final publication. Citation information: DOI 10.1109/ACCESS.2018.2855060, IEEE Access

$$\frac{\partial \phi}{\partial t} = -\delta(\phi)\left(\lambda_1 e_1 - \lambda_2 e_2 - \nu div\left(\frac{\nabla \phi}{|\nabla \phi|}\right)\right) + \gamma\left(\nabla^2 \phi - div\left(\frac{\nabla \phi}{|\nabla \phi|}\right)\right) \quad (7)$$

where div is the divergence operator, and e_1 and e_2 are functions defined as

$$e_1(x) = \int_\Omega K_\sigma(y-x)|I(x) - f_1(y)|^2 dy \quad (8)$$

$$e_2(x) = \int_\Omega K_\sigma(y-x)|I(x) - f_2(y)|^2 dy \quad (9)$$

The RSF model has the advantage of accurately segmenting the images with intensity inhomogeneity. However, the segmentation requires more iterations and consumes more time for a poor initial contour because the RSF model largely relies on the initialization of the contour. Moreover, the model is prone to fall into local minimum owing to the non-convexity of its energy function if the initial position of the contour is set far away from the actual boundary.

B. THE LIF MODEL

The LIF energy function is introduced by minimizing the difference between the fitted and original images [25][26].

$$E^{LIF}(\phi) = \frac{1}{2}\int_\Omega |I(x) - I^{LFI}(x)|^2 dx, \quad x \in \Omega \quad (10)$$

I^{LFI} is given as following:

$$I^{LFI} = m_1 H_\varepsilon(\phi) + m_2(1 - H_\varepsilon(\phi)) \quad (11)$$

where m_1 and m_2 are defined as follows:

$$m_1 = mean(I \in (\{x \in \Omega \mid \phi(x) < 0\} \cap W_k(x))) \quad (12)$$

$$m_2 = mean(I \in (\{x \in \Omega \mid \phi(x) > 0\} \cap W_k(x))) \quad (13)$$

where $W_k(x)$ is a rectangular window function with standard deviation σ. The function has a size of $4k+1$ by $4k+1$, where k is the nearest integer to σ. By using the calculus of variation and steepest descent method, $E^{LIF}(\phi)$ can be minimized with respect to the corresponding gradient descent flow.

$$\frac{\partial \phi}{\partial t} = (1 - I^{LFI})(m_1 - m_2)\delta_\varepsilon(\phi) \quad (14)$$

The LIF model is similar to the RSF model, in which the local intensity information is used to segment the image. Unlike the RSF model, for minimizing the energy function, image segmentation is achieved by minimizing the difference between the local fitted image and original image; thus, the LIF model is less sensitive to the settings of the initial contour.

III. HYBRID ACTIVE CONTOUR SEGMENTATION

In this section, we propose a hybrid method combining the RSF model and LIF model to improve the segmentation accuracy for D-SPECT images.

A. ACTIVE CONTOURS WITH LOCAL IMAGE FITTING ENERGY

The energy of each point $x \in \Omega$ is mathematically given as below:

$$E_x = \int K_\sigma(x-y)|I(y) - [f_1(x)H(\phi(y)) + f_2(x)(1 - H(\phi(y)))]|^2 dy \quad (15)$$

where K is a weighting function with a localization property that $K(v)$ decreases and approaches to zero as $|v|$ increases. $f_1(x)$ and $f_2(x)$ are two numbers that fit image intensities near the point x. $H(y)$ is the Heaviside function. Meanwhile, the point is described as the centre point of the above integral, and the energy E_x is defined as the local image fitting (LIF) energy. $E_x^{LIF}(C, f_1(x), f_2(x))$ is used to represent (15) because the contour C, the centre point x, and two fitting values $f_1(x)$ and $f_2(x)$ influence the energy E_x. E_x and $E_x^{LIF}(C, f_1, f_2)$ is minimized by the numbers f_1 and f_2, which vary with the centre point x.

In our study, a Gaussian kernel is used to describe the weighting function $K(x)$, where $\sigma > 0$ is a scale parameter.

$$K_\sigma(x) = \frac{1}{(2\pi)^{\frac{n}{2}}\sigma} e^{-\frac{|x|^2}{2\sigma^2}} \quad (16)$$

The values of f_1 and f_2 are influenced apparently by the image intensities at the points y near the centre point x, because the weighting function $K(x-y)$ takes larger values at the points y near the point x and decreases to zero as y goes away from x. By contrast, because $K(x-y)$ approaches zero for a large distance $|x-y|$, the values of f_1 and f_2 are scarcely influenced by the image intensities at the points y far away from the point x. The fitting energy in (15) is localized in the sense that the values f_1 and f_2 only fit the image intensities near each centre point x in the proposed model, owing to the spatially varying weighting function K with the above localization property. Moreover, when the fitting values f_1 and f_2 are chosen optimally and the contour C is exactly on the object boundary, the local fitting energy E_x^{LIF} is minimized for each centre point x.

However, E_x^{LIF} as defined above is local for a centre point $x \in \Omega$. E_x^{LIF} is minimized for all the centre points x in the image domain Ω in order to find the entire object boundary. It can be achieved by minimizing the integral of all the centre points in the image domain Ω. The external energy that is computed from the image data is given by the equation

$$E(C, f_1, f_2) = \int_\Omega E_X^{LIF}(C, f_1(x), f_2(x))dx \quad (17)$$

This article has been accepted for publication in a future issue of this journal, but has not been fully edited. Content may change prior to final publication. Citation information: DOI 10.1109/ACCESS.2018.2855060, IEEE Access

B. VARIATIONAL LEVEL SET FORMULATION OF THE MODEL

In level set approaches, a contour $C \subset \Omega$ is represented by the zero level set of a Lipschitz function $\phi : \Omega \to \Re$. With the level set representation, the energy functional can be rewritten as

$$E^{LIF}(\phi, f_1, f_2) = \int_\Omega E_X^{LIF}$$

$$= \iint_\Omega K_\sigma(x-y)\left|I(y) - [\, f_1(x)H(\phi(y)) + f_2(x)(1-H(\phi(y)))]\right|^2 dydx \tag{18}$$

The distance regularizing term is added in order to ensure stable evolution of the level set function ϕ. The deviation of the level set function ϕ from a signed distance function is given as follows:

$$D(\phi) = \int_\Omega \frac{1}{2}\left(|\nabla\phi(x)| - 1\right)^2 dx \tag{19}$$

The length of the zero level curve of ϕ, which is used to regularize the zero level contour of ϕ is expressed as follows:

$$L(\phi) = \int_\Omega \delta(\phi(x))|\nabla\phi(x)|\, dx \tag{20}$$

The entire energy functional is then given by the following equation, where β and μ are nonnegative constants.

$$F(\phi, f_1, f_2) = E^{LIF}(\phi, f_1, f_2) + \beta D(\phi) + \mu L(\phi) \tag{21}$$

To achieve good approximation of H and δ by H_ε and δ_ε, ε is set to 1.0 in the equations (3) (4). The energy functions E^{LIF} and L are regularized as E_ε^{LIF} and L_ε by replacing H and δ in (18) and (20) with H_ε and δ_ε. Thus, the energy function can be approximated as

$$F_\varepsilon(\phi, f_1, f_2) = E_\varepsilon^{LIF}(\phi, f_1, f_2) + \beta D(\phi) + \mu L_\varepsilon(\phi) \tag{22}$$

The energy function above is minimized to find the object boundary.

C. GRADIENT DESCENT FLOW

Keeping the level set function ϕ fixed and minimizing the energy functional $F_\varepsilon(\phi, f_1, f_2)$ with regard to functions $f_1(x)$ and $f_2(x)$, $f_1(x)$ and $f_2(x)$ can be obtained through a partial derivative of x.

$$f_1(x) = \frac{K_\sigma(x) * [H_\varepsilon(\phi(x))I(x)]}{K_\sigma(x) * H_\varepsilon(\phi(x))} \tag{23}$$

$$f_2(x) = \frac{K_\sigma(x) * [(1-H_\varepsilon(\phi(x)))I(x)]}{K_\sigma(x) * [1-H_\varepsilon(\phi(x))]} \tag{24}$$

Because $H_\varepsilon > 0$ and $1 - H_\varepsilon > 0$ through the definition of H_ε, the denominators in (23) and (24) are always positive.

Next, the energy functional $F_\varepsilon(\phi, f_1, f_2)$ is minimized with regard to a level set function ϕ for fixed functions $f_1(x)$ and $f_2(x)$.

$$\frac{\partial\phi}{\partial t} = -\delta_\varepsilon(\phi)\int K_\sigma(x-y)[I(y) - (f_1(x)H(\phi(y))) + f_2(x)(1-H(\phi(y)))](f_1(x) - f_2(x))dy$$

$$+ \beta\left(\nabla^2\phi - div\left(\frac{\nabla\phi}{|\nabla\phi|}\right)\right) + \mu\delta_\varepsilon(\phi)div\left(\frac{\nabla\phi}{|\nabla\phi|}\right) \tag{25}$$

The above equation (25) is the proposed model in our study.

IV. RESULTS

A. SUBJECTIVE EVALUATIONS OF EXPERIMENTAL RESULTS

This article has been accepted for publication in a future issue of this journal, but has not been fully edited. Content may change prior to final publication. Citation information: DOI 10.1109/ACCESS.2018.2855060, IEEE Access

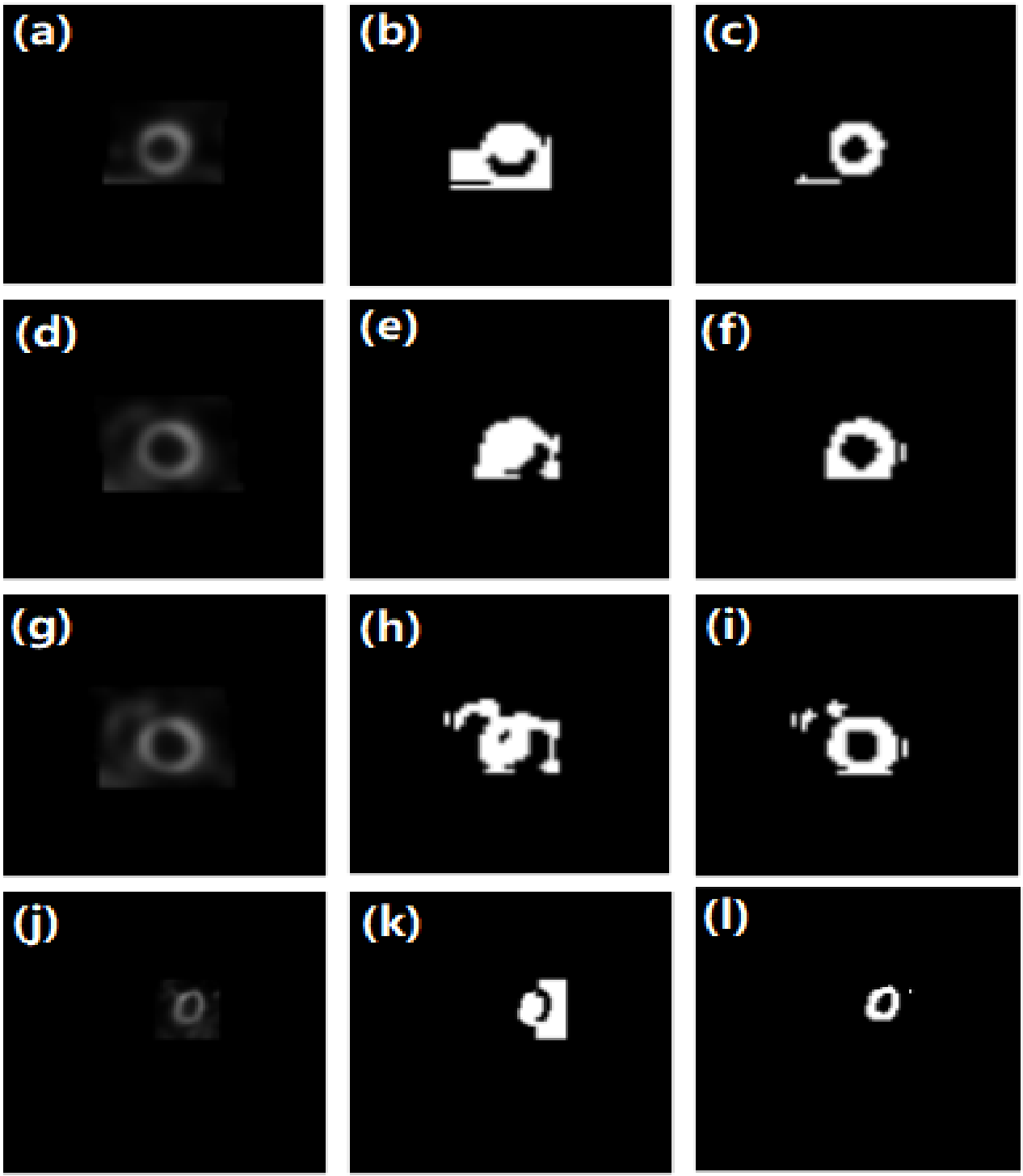

FIGURE 3. A series of contrasting experiments on short-axis images. (a), (d), (g) and (j) are the original images. (b), (e), (h) and (k) are the segmentation results based on the RSF model, while (c), (f), (i) and (l) are the segmentation results based on our proposed model.

This article has been accepted for publication in a future issue of this journal, but has not been fully edited. Content may change prior to final publication. Citation information: DOI 10.1109/ACCESS.2018.2855060, IEEE Access

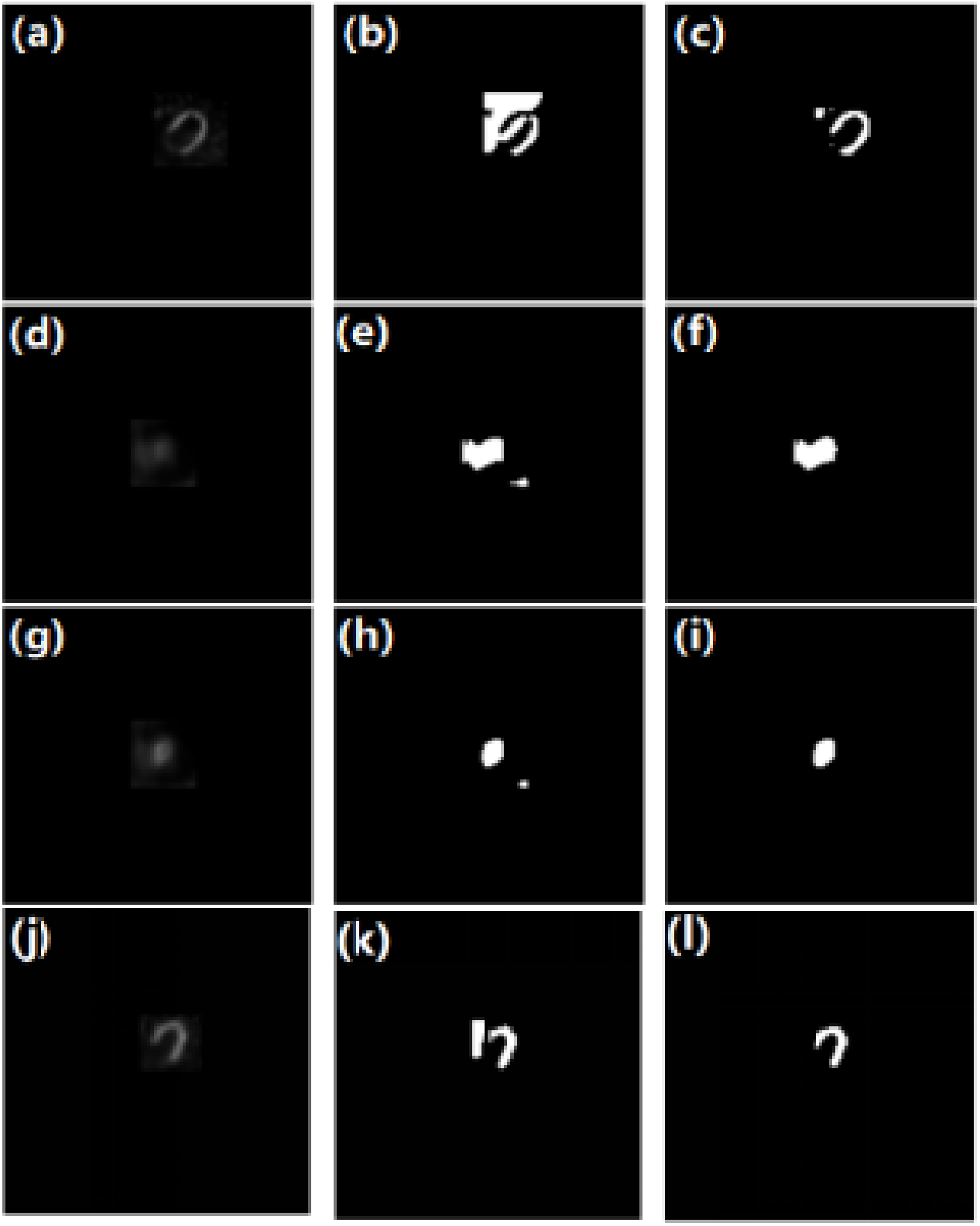

FIGURE 4. A series of contrasting experiments on long-axis images. (a), (d), (g) and (j) are the original images. (b), (e), (h) and (k) are the segmentation results based on the RSF model, while (c), (f), (i) and (l) are the segmentation results based on our proposed model.

This article has been accepted for publication in a future issue of this journal, but has not been fully edited. Content may change prior to final publication. Citation information: DOI 10.1109/ACCESS.2018.2855060, IEEE Access

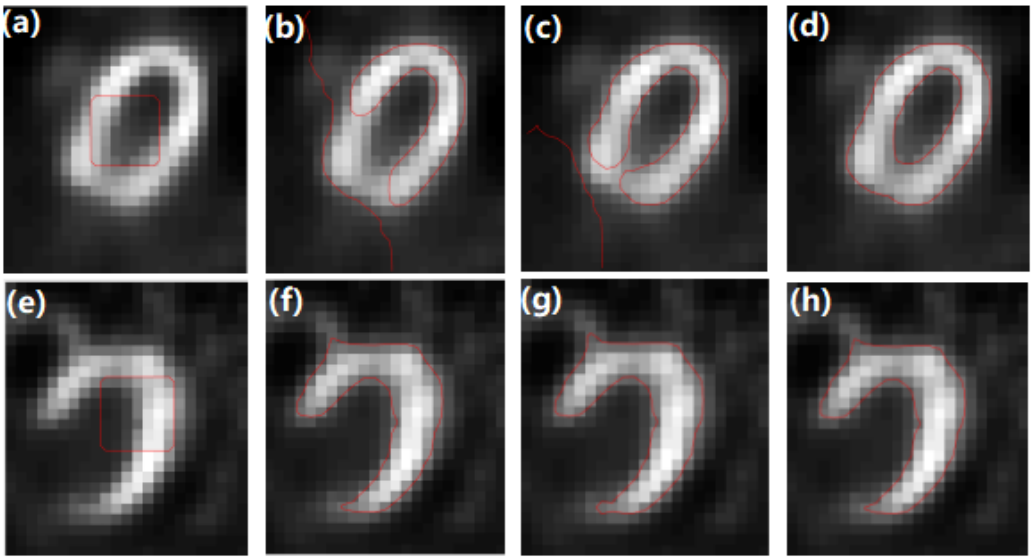

FIGURE 5. Evolution of contour curve of our proposed model. (a) to (d) respectively show the initial contour, 20 iterations, 100 iterations, and final contour of short-axis images. (e) to (h) respectively show the initial contour, 200 iterations, 400 iterations, and final contour of long-axis images.

A series of segmentation results on short-axis and long-axis images based on the RSF model and our proposed model are shown in Fig. 3 and Fig. 4, respectively. It can be seen that the segmentation results based on our proposed model are more precise than those based on the RSF model, where fewer redundant segmentation results occur. Furthermore, the evolution of contour curve based on our proposed model is shown in Fig. 5. In Fig. 5, irrespective of whether the images are long-axis or short-axis images, the segmentation results become more accurate with the increase in the number of iterations.

B. OBJECTIVE EVALUATIONS OF EXPERIMENTAL RESULTS

A set of metrics is used to measure the accuracy of the proposed automatic method for segmentation, considering the manual segmentation as a reference. The measures are mathematically expressed as follows:

a) Jaccard similarity coefficient (JS)

$$JS = \frac{|S_G \cap S_M|}{|S_G \cup S_M|} \tag{28}$$

b) Dice similarity coefficient (DSC)

$$DSC = 2 \cdot \frac{|S_G \cap S_M|}{|S_G| + |S_M|} \tag{29}$$

c) True positive rate (TPR)

$$TPR = \frac{|S_G \cap S_M|}{|S_G|} \tag{30}$$

d) False positive rate (FPR)

$$FPR = \frac{|S_G \cup S_M - S_M|}{|S_G|} \tag{31}$$

where S_G stands for the foreground of the ground truth image and S_M indicates the foreground obtained by the models.

TABLE I
PERFORMANCE EVALUATIONS ON IMAGES OF LONG-AXIS MATTER SEGMENTATION QUALITY BETWEEN DIFFERENT METHODS

Metric		DSC	JS	TPR	FPR
Set 1	RSF	0.8835	0.8835	0.8835	0.8835
	Our model	0.8916	0.8916	0.8916	0.8916
Set 2	RSF	0.8724	0.8724	0.8724	0.8724
	Our model	0.8804	0.8804	0.8804	0.8804
Set 3	RSF	0.8879	0.8879	0.8879	0.8879
	Our model	0.8957	0.8957	0.8957	0.8957
Set 4	RSF	0.8721	0.8721	0.8721	0.8721
	Our model	0.8765	0.8765	0.8765	0.8765
Set 5	RSF	0.8906	0.8906	0.8906	0.8906
	Our model	0.8981	0.8981	0.8981	0.8981
Set 6	RSF	0.7864	0.7864	0.7864	0.7864
	Our model	0.8233	0.8233	0.8233	0.8233

This article has been accepted for publication in a future issue of this journal, but has not been fully edited. Content may change prior to final publication. Citation information: DOI 10.1109/ACCESS.2018.2855060, IEEE Access

TABLE Ⅱ
PERFORMANCE EVALUATIONS ON IMAGES OF SHORT-AXIS MATTER SEGMENTATION QUALITY BETWEEN DIFFERENT METHODS

Metric	Set 1		Set 2		Set 3		Set 4		Set 5	
	RSF model	Our model	RSF model	Our model	RSF model	Our model	RSF model	Our model	RSF model	Our model
DSC	0.7436	0.7946	0.737	0.806	0.8471	0.8613	0.7924	0.8509	0.9378	0.9426
JS	0.6294	0.6795	0.5929	0.677	0.7353	0.7567	0.675	0.741	0.8828	0.8915
TPR	0.8425	0.8858	0.7377	0.8338	0.8663	0.8925	0.7766	0.8338	0.9339	0.9504
FPR	0.1575	0.1142	0.2623	0.1662	0.1337	0.1075	0.2234	0.1662	0.0661	0.0496

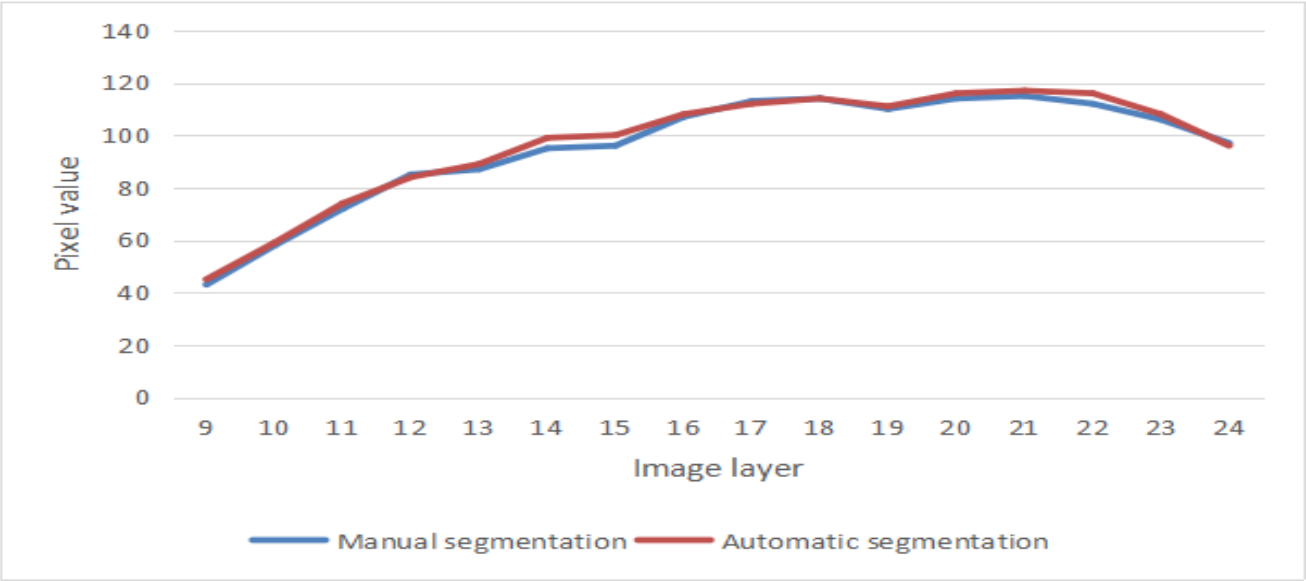

FIGURE 6. Evaluation of segmentation accuracy.

Performance evaluations on long-axis and short-axis images are shown in Table Ⅰ and Table Ⅱ, respectively. It can be demonstrated that our model performs better than the RSF model does in DSC, JS, TPR, and FPR.

The pixel values of segmentation regions are shown in Fig. 6, where manual segmentation and automatic segmentation are included. It can be seen that when the image layers range from 9 to 24, the pixel values of manual segmentation and automatic segmentation are approximately equal.

V. CONCLUSION

In this study, we proposed a new hybrid model for automatic myocardium D-SPECT images segmentation. In the model, two fitting functions are used to fit the grey level inside and outside the curve. The new model is robust on the initialization of the contour. A set of experiments demonstrate the accuracy of output segmentation results. The method solved the issues of image artefacts and inaccuracy of instruments, which can lead to intensity inhomogeneity in the image. In future, more local information of the image will be introduced into the energy functional of the proposed model to further improve the segmentation accuracy. In addition, the model will be implemented using narrow-band techniques to increase the computational speed.

REFERENCES

[1] Seokyoon Choi, Hochul kim, and Jangseok Oh, "Segmentation of the Left ventricle in Myocardial Perfusion SPECT Using Variational Level set Formulation," IEEE Nuclear Science Symposium Conference Record, 2007.

[2] T. McInerney and D. Terzopoulos, "Deformable models in medical image Analysis," A Survey Medical Image Analysis, vol. 1, no. 2, pp. 91-108, 1996.

[3] N. Paragios, "A Variational Approach for the Segmentation of the Left Ventricle in MR Cardiac Images," International Journal of Computer Vision, vol. 50, no. 22, pp. 345-362, 2002.

[4] Pierre-Marc Jodoin, Fredy Pinheiro, Alexandra Oudot, and Alain Lalande, "Left-Ventricle Segmentation of SPECT Images of Rats," IEEE T BIO-MED ENG, vol. 62, no. 9, Sep. 2015.
[5] Poujol, J., Desvignes, M., et al., "Myocardium segmentation on 3d spect images," ICIP 2015, pp. 4788-4792, 2015.
[6] T. Chan and L. Vese, "Active contours without edges," IEEE Trans. Image. Proc, vol. 10, pp. 266-277, 2001.
[7] Chan, T. and Vese, L., "An active contour without edges," Scale-Space '99, M. Nilsen et al., LNCS, vol. 1682, 1999.
[8] M. Kass, A. Witkin, D. Terzopoulos, "Snakes: active contour models," Int. J. Vis., vol. 1, no. 4, pp. 321-331, 1987.
[9] D. Cremers, M Rousson, R. Deriche, "A review of statistical approaches to level set segmentation: integrating color, texture, motion and shape," Int. J. Comput. Vis., vol. 72, no. 2, pp. 195-215, 2007.
[10] Z. Ma, J.M.R.S Tavares, "A review of algorithms for medical image segmentation and their applications to the female pelvic cavity," Comput. Methods Biomech. Biomed. Eng., vol. 131, pp. 235-246, 2010.
[11] R. B. Oliveira, M.E. Filho, Z. Ma, et al., "Computational methods for the image segmentation of pigmented skin lesions: a review, " Comput. Meth. Programs Biomed., vol. 13, no. 2, pp. 235-246, 2016.
[12] G. Guisong Xia, W. Liu, et al., "Object segmentation from SAR images via a multiscale non-local active contour model," IEEE Trans. Geosci. Remote Sens., vol. 54, no. 3, pp. 1860-1873, 2016.
[13] V. Gaselles, R. Kimmel, G. Sapiro, "Geodesic active contours," Int. J. Comput. Vis., vol. 22, no. 1, pp. 61-79, 1997.
[14] Qiang Li, Tingquan Deng, Wei Xie, "Active contours driven by divergence of gradient vector flow," Signal Process, vol. 120, pp. 185-199, 2016.
[15] Guoqi Liu, Zhiheng Zhou, and Shengli Xie, "Global minimization of adaptive local image fitting energy for image segmentation," J SYST ENG ELECTRON, vol. 25, no. 2, pp. 307-313, Apr. 2014.
[16] Bin Han, and Yiquan Wu, "A novel active contour model based on modified symmetric cross entropy for remote sensing river image segmentation," Pattern Recognition, vol. 67, pp. 396-409, 2017.
[17] B.N. Li, C.K. Chui, S. Change, et al., "Integrating spatial fuzzy clustering with level set methods for automated medical image segmentation," Comput. Biol. Med., vol. 41, no. 1, pp. 1-10, 2011.
[18] F. Dong, Z. Chen, J. Wang, "A new level set method for inhomogeneous image segmentation," Image Vis. Comput., vol. 31, no. 10, pp. 809-822, 2013.
[19] Hui Wang, Tingzhu Huang, Zongben Xu, et al., "An active contour model and its algorithms with local and global Gaussian distribution fitting energies," Information Sciences, vol. 263, pp. 43-59, 2014.
[20] K. Zhang, L. Zhang, H. Song, W. Zhou, "Active contours with selective local or global segmentation: a new formulation and level set method," Image Vis. Comput., vol. 28, no. 4, pp. 668-676, 2010.
[21] L. Cohen and I. Cohen, "Finite-element methods for active contour models and balloons for 2-D and 3-D images," IEEE Trans. Patt. Anal. Mach. Intell., vol. 15, pp. 1131-1147, 1993.
[22] A. Tasi, A. Yezzi and A. S. Willsky, "Curve evolution implementation, denoising, interpolation, and magnification," IEEE Trans. Imag. Proc., vol. 10, pp. 1169-1186, 2001.
[23] A. Tsai, A. J. Yezzi, W. M. W. III, C. Tempany, D. Tucker, A. Fan, W. E. L. Grimson, and A. S. Willsky, "A shape-based approach to the segmentation of medical imagery using level sets," IEEE Trans. Med. Imaging, vol. 22, pp. 137-154, 2003.
[24] Zhi Xu, Ting-Zhu Huang, Hui Wang and Chuanlong Wang, "Variant of the region-scalable fitting energy for image segmentation," J OPT SOC A, vol. 32, no. 3, Mar. 2015.
[25] Lei Wang, Yan Chang, et al., "An active contour model based on local fitted images for image segmentation," Information Sciences, vol. 418, pp. 61-73, Jun. 2017.
[26] Kaihua Zhang, Huihui Song, and Lei Zhang, "Active contours driven by local image fitting energy," Pattern Recognition, vol. 43, pp. 1199-1206, 2010.